



Article

Self-Powered Nitrogen Dioxide Sensor Based on Pd-Decorated ZnO/MoSe₂ Nanocomposite Driven by Triboelectric Nanogenerator

Weiwei Wang, Dongyue Wang, Xixi Zhang, Chunqing Yang and Dongzhi Zhang *

College of Control Science and Engineering, China University of Petroleum (East China), Qingdao 266580, China
* Correspondence: dzzhang@upc.edu.cn

Abstract: This paper introduces a high-performance self-powered nitrogen dioxide gas sensor based on Pd-modified ZnO/MoSe₂ nanocomposites. Poly(vinyl alcohol) (PVA) nanofibers were prepared by high-voltage electrospinning and tribological nanogenerators (TENGs) were designed. The output voltage of TENG and the performance of the generator at different frequencies were measured. The absolute value of the maximum positive and negative voltage exceeds 200 V. Then, the output voltage of a single ZnO thin-film sensor, Pd@ZnO thin-film sensor and Pd@ZnO/MoSe₂ thin-film sensor was tested by using the energy generated by TENG at 5 Hz, when the thin-film sensor was exposed to 1–50 ppm NO₂ gas. The experimental results showed that the sensing response of the Pd@ZnO/MoSe₂ thin-film sensor was higher than that of the single ZnO film sensor and Pd@ZnO thin-film sensor. The TENG-driven response rate of the Pd@ZnO/MoSe₂ sensor on exposure to 50 ppm NO₂ gas was 13.8. At the same time, the sensor had good repeatability and selectivity. The synthetic Pd@ZnO/MoSe₂ ternary nanocomposite was an ideal material for the NO₂ sensor, with excellent structure and performance.

Keywords: TENG; self-powered; NO₂ gas sensor; ternary nanocomposite



Citation: Wang, W.; Wang, D.; Zhang, X.; Yang, C.; Zhang, D. Self-Powered Nitrogen Dioxide Sensor Based on Pd-Decorated ZnO/MoSe₂ Nanocomposite Driven by Triboelectric Nanogenerator. *Nanomaterials* **2022**, *12*, 4274. <https://doi.org/10.3390/nano12234274>

Academic Editor:
Antonella Macagnano

Received: 22 October 2022
Accepted: 28 November 2022
Published: 1 December 2022

Publisher's Note: MDPI stays neutral with regard to jurisdictional claims in published maps and institutional affiliations.



Copyright: © 2022 by the authors. Licensee MDPI, Basel, Switzerland. This article is an open access article distributed under the terms and conditions of the Creative Commons Attribution (CC BY) license (<https://creativecommons.org/licenses/by/4.0/>).

1. Introduction

Nitrogen oxide (NO₂) is an important component on air pollutants, which has a serious impact on human health. Among them, the exhaust gas from motor vehicles and power plants in industry releases more nitrogen dioxide gas [1]. NO₂ can stimulate people's respiratory tract, reduce the resistance of the respiratory tract and induce various inflammation of the respiratory tract. Moreover, it participates in photochemical reactions and forms acid rain, which is harmful to ground organisms and human health [2]. Therefore, the sensitive NO₂ gas sensor has attracted wide attention [3]. So far, in various sensing technologies, many scholars have used metal oxide semiconductors (such as WO₃, ZnO, CuO, In₂O₃) to prepare gas sensors [4–6]. However, most metal oxides have great requirements for temperature conditions when detecting NO₂, so it is necessary to develop a NO₂ sensor at room temperature. ZnO has unique properties and has broad application prospects in sensors, thin-film transistors, light-emitting diodes and other fields. It is sensitive to NO₂ gas at RT and widely used as a sensing material. The catalysis of noble metal can reduce the activation energy of the reaction, greatly improving the selectivity and sensitivity of gas sensors [7]. It is particularly important to develop sensors with high sensitivity, low cost and miniaturization. The interdigital electrode can be used for various miniaturized sensors because of its tiny electrode spacing structure. Traditional analytical detection, including chromatography, spectroscopy, mass spectrometry and other methods, mostly need expensive instruments and a variety of operating steps, leading to many practical problems and difficulties. At the same time, the interdigital electrode is a parallel circuit, which can increase the response to the test signal and reduce the manufacturing cost of the sensor.

In recent years, wind power, hydropower and solar power have brought great convenience to people's life, but they are more vulnerable to the weather, bulky and not easy to carry [8]. In 2012, Professor Wang also proposed triboelectric nanogenerators (TENGs) [9]. A nanogenerator has a simple structure and low cost and can collect energy from the environment. In recent years, nanogenerators have been widely studied and many achievements have been made in applications [10,11]. The TENG is usually composed of triboelectric pairs and corresponding conductive electrodes. The potential is generated during friction. In order to make the potential equal, the charge (electron or ion/molecule) will move between the two materials [12–14]. Common friction materials, such as polytetrafluoroethylene (PTFE), polyimide film (PI), polydimethylsiloxane (PDMS) and so on, have been widely used in TENGs [15]. With the continuous development of science and technology, nanogenerators can be combined with sensors to realize the development of self-powered sensors, which provides new insights for the development of sensors [16,17].

In this work, PVA was synthesized on aluminum foil (Al-PVA) by electrospinning and a nanogenerator was prepared by using Al-PVA and PI as friction materials. What is more, using it for a Pd@ZnO/MoSe₂-based NO₂ gas sensor provides power at 25 °C. In this paper, the voltages of TENGs at different frequencies were measured. The TENG was used as the power supply. The sensing performance of the NO₂ sensor was investigated towards NO₂ gas. Compared with single ZnO and Pd@ZnO, the sensing properties of Pd@ZnO/MoSe₂ were improved obviously.

2. Experimental

2.1. Materials

Reagents used in the experiments mainly included zinc nitrate hexahydrate (Zn(NO₃)₂·6H₂O), sodium dodecyl sulfate (SDS), polyvinyl alcohol (PVA), palladium chloride (PdCl₂), sodium hydroxide (NaOH), sodium molybdate dihydrate (Na₂MoO₄·2H₂O), selenium powder (Se), sodium borohydride (NaBH₄), ethanol and hydrazine hydrate, which were obtained from Sinopharm Chemical Reagent Co. Ltd.

2.2. Material Synthesis

Electrospinning synthesis of PVA: 3.9 g PVA was added into 30 mL DI water under stirring for 30 min at 25 °C, and 0.1 g SDS powder was added into the above solution. The SDS is beneficial to the formation of nanofibers [18,19]. The 11 wt% of PVA solution was continuously stirred at 90 °C for 6 h. Al substrate was attached to the disc to collect the electrospun fiber film [20]. PVA nanofiber network has certain viscoelasticity and can recover after deformation, so the TENG can maintain good frictional durability.

Synthesis of ZnO nanoparticles (NPs): 2.08 g Zn(NO₃)₂·6H₂O was added to 140 mL deionized (DI) water and stirred for 30 min at 25 °C. Then, 3.2 g NaOH was dissolved into 20 mL DI water to prepare 4 mol/L aqueous solution. Then the two aqueous solutions were mixed under continuous stirring for 1 h and ultrasonic vibration for 15 min. Subsequently, the mixed solution was transferred into an autoclave and heated at 120 °C for 12 h. Finally, the ZnO nanoparticles were obtained by centrifugation and washing with DI water and dried at 60 °C overnight.

Synthesis of Pd@ZnO NPs: Certain amounts of PdCl₂, hydrazine hydrate (20 µL) and NaOH (50 mg) were dissolved in 80 mL DI water under continuous stirring for 1 h, and hydrazine hydrate was used to obtain reduced palladium from PdCl₂. Then, the prepared ZnO was added into the above solution and heated in an autoclave at 180 °C for 10 h. Finally, the Pd@ZnO product was treated by centrifugation and washing with DI water and dried at 60 °C overnight [21].

Synthesis of Pd@ZnO/MoSe₂ film sensor: MoSe₂ nanoflowers were synthesized by solvothermal reaction. Na₂MoO₄·2H₂O (0.6 g) and NaBH₄ (0.1 g) were dissolved in a mixed solution of 25 mL deionized water and 25 mL ethanol. Then, 10 mL of hydrazine hydrate solution containing 0.493 g selenium powder was poured into the above solution and stirred violently at 25 °C for 2 h. Then, the solution was put into a reactor and heated

at 200 °C for 48 h. The black MoSe₂ powder was finally collected by washing with ethanol and deionized water several times and dried overnight at 60 °C. The precipitate was washed with deionized water and methanol, and the unreacted monomer was removed with acetone many times. To obtain Pd@ZnO/MoSe₂ solution, 0.2 g MoSe₂ powder was added to the pre-prepared Pd@ZnO solution under continuous ultrasonic dispersion for 1 h. Finally, the solution was dripped onto the interdigital electrode and dried at 60 °C for 4 h to form a sensing film. The detailed manufacturing process of the thin-film sensor is shown in Figure 1a. The interdigital electrodes (IDEs) were prepared by sputtering, photolithography and development. As shown in Figure 1b, the gas-sensing materials were deposited on the IDEs via spraying. The dimension of IDEs is 8 × 8 mm and the thickness is 300 μm. The NO₂ gas-sensing characteristics of the sensor were investigated by studying the response, response/recovery time and selectivity of the sensor. A diagram of the test system is shown in Figure 1c. The sensor as a load was plugged into the TENG circuit. The sensor response can be defined as follows: $\text{Response} = V_g/V_a$, where V_a and V_g represent the voltage across the sensor when the sensor is in air and NO₂ gas, respectively. The response/recovery time at a specific concentration is defined as the time for sensor to achieve 90% of maximum response.

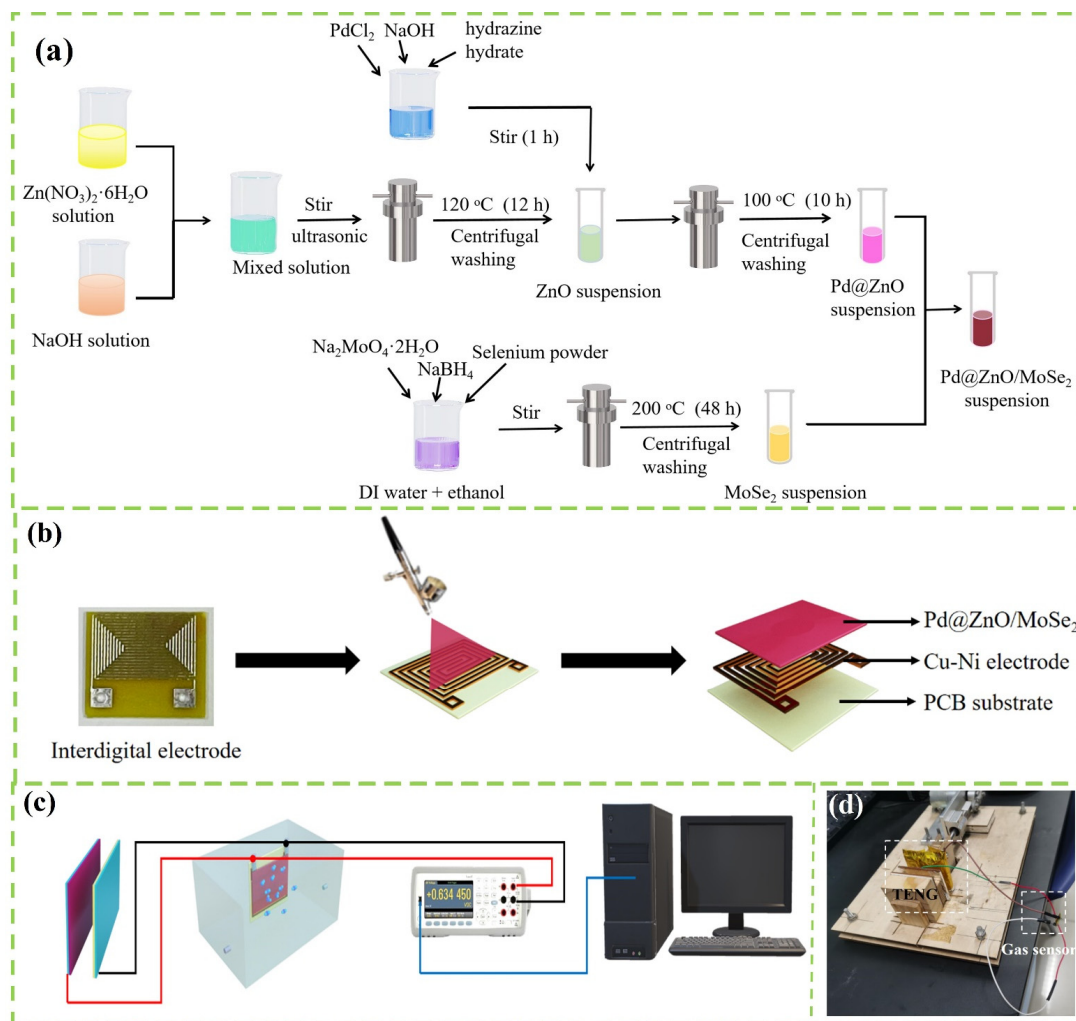


Figure 1. Manufacturing process of (a) Pd@ZnO/MoSe₂ and (b) gas sensor. (c) A diagram of the test system. (d) A picture of the TENG and the sensing device powered with TENG.

2.3. Sensor Assembly

Figure 2a shows the design structure of the Al-PVA/PI triboelectric nanogenerator. The structure of TENG mainly consists of two parts: one is electrode and the other is friction material. Al layer acted as electrode, PVA was covered on Al electrode and polyimide film was regarded as friction layer. The nanogenerator was used to drive the synthesized NO₂ sensor, in which the sensing characteristics of the thin-film sensor were tested on exposure to NO₂ gas at 25 °C. In order to test the voltage signal and the gas response signal, the device was connected with the key 34,470 A.

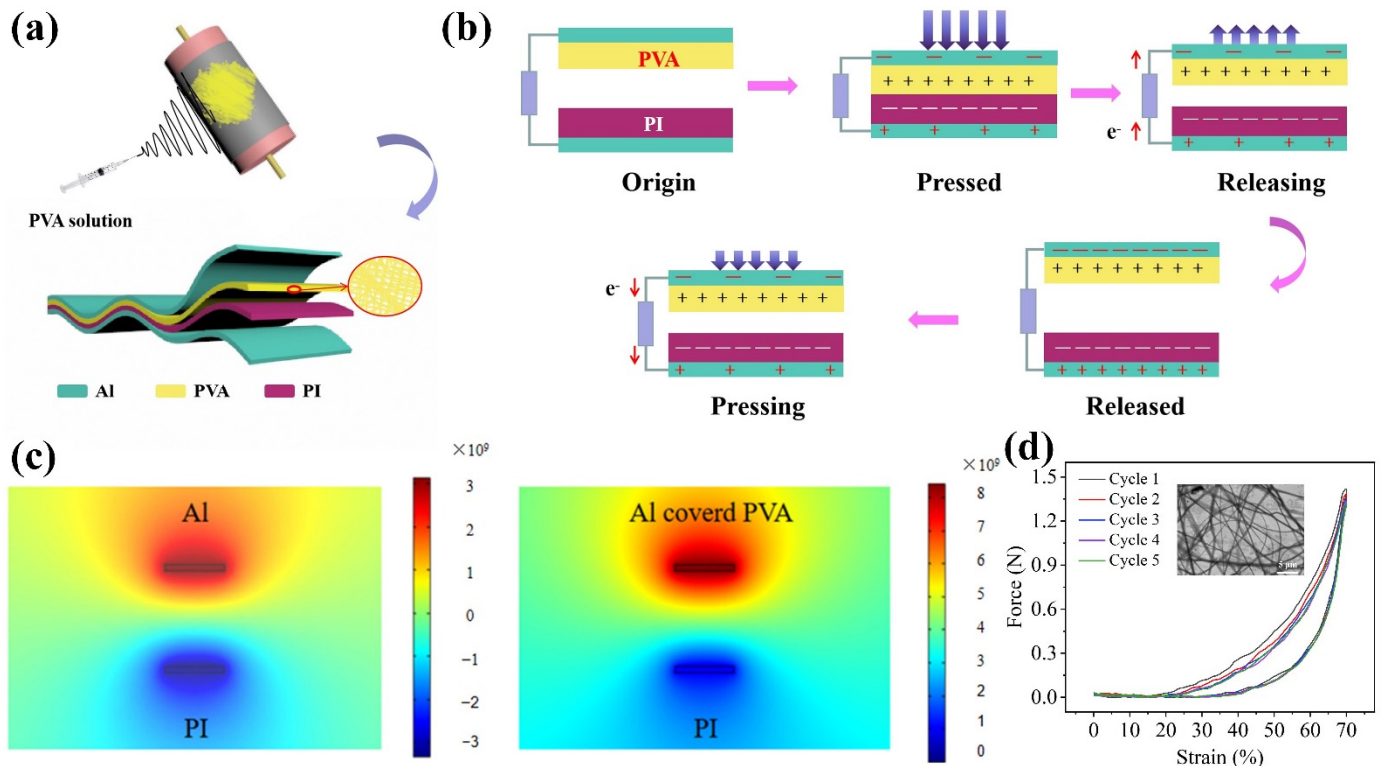


Figure 2. (a) Structure of Al-PVA/PI TENG and manufacturing process. (b) Schematic diagram of operating principle of generator. (c) Effect of TENG friction potential. (d) Hysteresis cycle of PVA on TENG surface.

2.4. Characterization Instrument

The morphology and microstructure of nanocomposites were studied by using a scanning electron microscope (SEM, HITACHI S-4800). X-ray diffraction (XRD) was measured to clarify phase composition and purity of samples on RIGAKU D/max 2500 PC. X-ray photoelectron spectroscopy (XPS; Thermo Scientific escalator 250Xi) was performed to investigate elemental composition and chemical valence states of Pd@ZnO/MoSe₂ samples.

3. Results and Discussion

3.1. Characterizations of TENG

Figure 2b illustrates a schematic diagram of the operating principle of the generator. According to the triboelectric sequence [12], PVA is more likely to lose electrons after contact with PI. In the original state, there is no potential difference between the two electrodes or induced charges. When the two films are separated, a potential difference is formed between the two films and drives electrons from the electrode on the PI to the electrode on the PVA via the external load. When two friction material surfaces contact again, a reverse current is generated. Figure 2c shows the effect of TENG friction potential studied by analysis and simulation using COMSOL software. Figure 2d illustrates the morphology

of PVA on the surface of the TENG. The PVA is mainly composed of nanofibers with an average diameter of 550 nm.

Figure 3a,b illustrate the dependence of output voltage, current and output power of the TENG on resistance. The results show that the output voltage increases with the increase in load resistance, while the output current is the opposite. The maximum output power can reach $17.5 \mu\text{W}$. Figure 3c shows that the mechanical properties of the TENG are relatively stable at 10 Hz, and the sum of absolute values of positive and negative maximum voltages is greater than 200 V. Figure 3d explains that the output voltage of TENG with PVA is much higher than that without PVA at 10 Hz, which is consistent with the simulation results. Compared with the pure Al film, the introduction of PVA nanofibers greatly improves the output performance of the TENG. PVA tends to lose electrons, which may generate more triboelectric charges. In addition, the nanofiber network structure improves the effective contact area of the material.

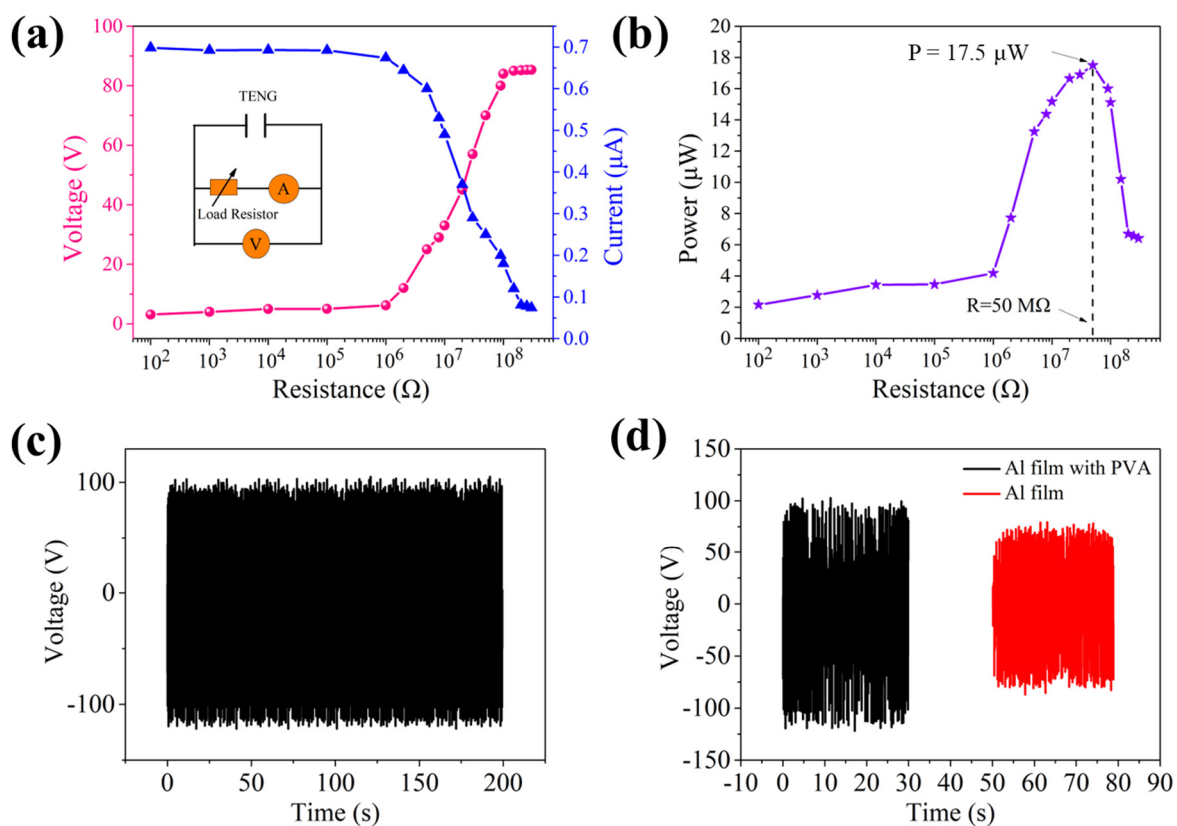


Figure 3. (a) Under the TENG, dependence of output voltage and current on external loading resistance. Insert is measurement circuit diagram. (b) Plot of output power versus loading resistance. (c) Repeatability of TENG at 10 Hz. (d) Comparison of output voltage of TENG with PVA and that without PVA at 10 Hz.

3.2. Sample Characterization

Figure 4a,b describe the SEM images of pure ZnO and MoSe₂ samples. Zinc oxide has a rod structure and the MoSe₂ sample is mainly composed of nanoflowers self-assembled by nanosheets. Figure 4c,d show the SEM images of Pd@ZnO/MoSe₂ composites. It can be observed that the composites have good contact with each other, which is conducive to obtaining a large number of gas-diffusion pathways.

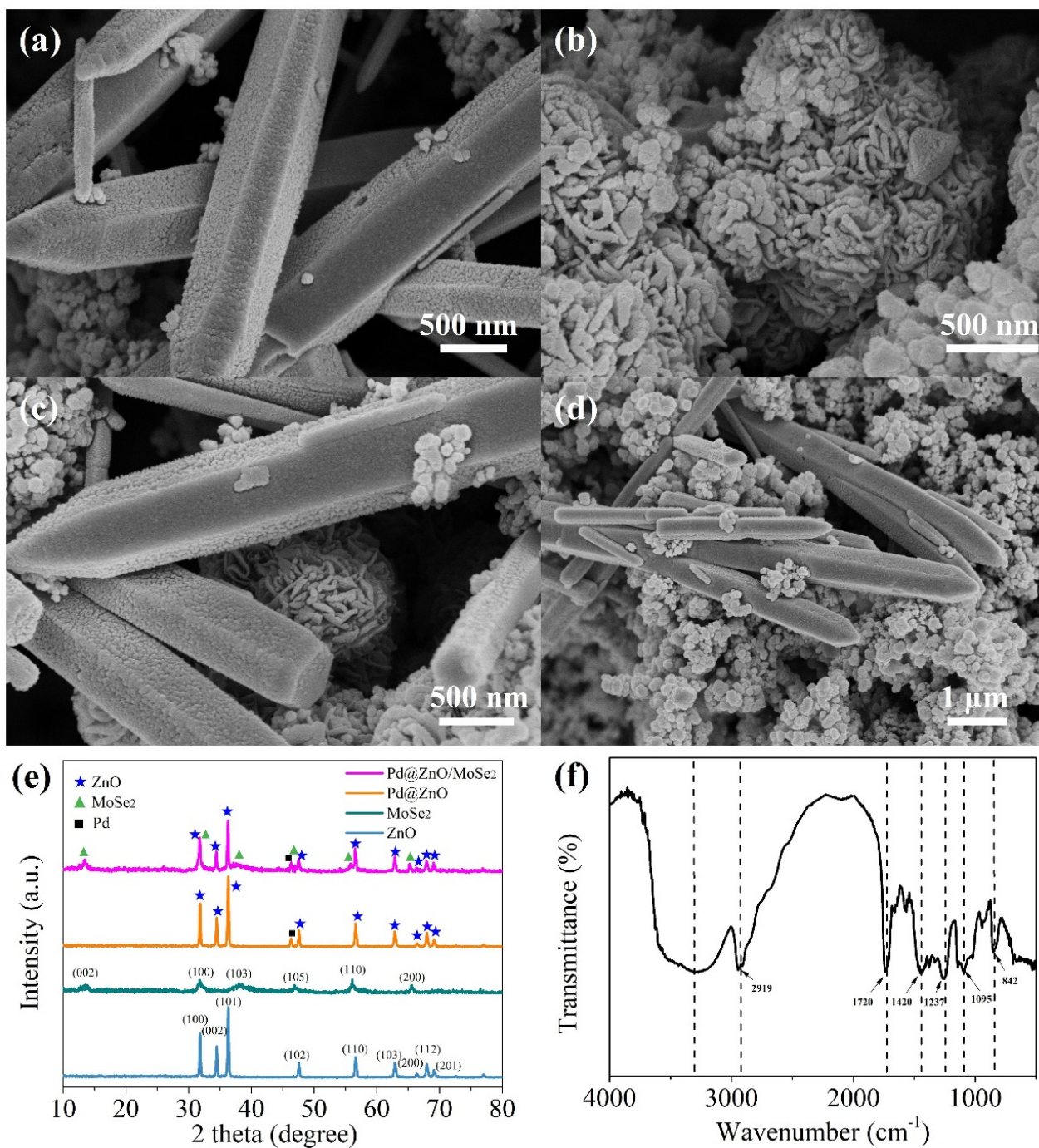


Figure 4. SEM images of (a) pure ZnO nanofibers, (b) pure MoSe₂ nanoflowers and (c,d) Pd@ZnO/MoSe₂. (e) FTIR spectrum of PVA samples. (f) XRD of ZnO, MoSe₂, Pd@ZnO and Pd@ZnO/MoSe₂ samples.

The FTIR spectrum of PVA nanofibers in a range of 4000–500 cm⁻¹ is shown in Figure 4e. The broad peak at 3338 cm⁻¹ is due to the stretching vibration of the O–H group of PVA. The peak at 2919 cm⁻¹ is attributed to the asymmetric stretching mode of C–H. The peak at 1720 cm⁻¹ is attributed to the bending vibration of C=O and the band at 1420 cm⁻¹ is attributed to C–H bending. The peaks at 1237, 1095 and 842 cm⁻¹ are attributed to C–C–O, C–O and C–C stretching, respectively [22]. Figure 4f illustrates the XRD spectra of ZnO, MoSe₂, Pd@ZnO and Pd@ZnO/MoSe₂ samples. For ZnO, the diffraction peaks at 31.8°, 34.3°, 36.3°, 47.6°, 56.6°, 62.9°, 66.3°, 67.9° and 69.1° are obviously observed, respectively, corresponding to (100), (002), (101), (102), (110), (103), (200), (112) and (201)

planes (JCPDS Card No. 36-1451) [23]. The diffraction peaks of MoSe₂ at 13.36°, 31.53°, 37.26°, 46.97°, 55.95° and 65.72° are shown, respectively, corresponding to (002), (100), (103), (105), (110) and (200) planes (JCPDS Card No. 29-0914) [20]. The diffraction peak of Pd@ZnO at 46.53° proves the existence of Pd [24]. The XRD pattern of Pd@ZnO/MoSe₂ nanocomposites contains the diffraction peaks of the three components, indicating the existence of Pd@ZnO/MoSe₂ nanocomposites.

The surface composition of the Pd@ZnO/MoSe₂ sample was further analyzed by XPS technology, as shown in Figure 5. The full spectrum of the Pd@ZnO/MoSe₂ sample in Figure 5a demonstrates that the sample is composed of the five elements of Pd, Zn, Mo, Se and O. Figure 5b shows the spectrum of Zn 2p. Two characteristic peaks at 1021.5 and 1044.3 eV, respectively, show the spin-orbit dipole splitting of Zn 2p_{1/2} and Zn 2p_{3/2}. Figure 5c shows the O1s spectrum. The characteristic peaks at 529.3 and 530.27 eV can be attributed to lattice oxygen (O_L) and ZnO-OH (O defect) in the Zn-O bond (O_V), and the characteristic peak at 531.8 eV can be attributed to the chemical-absorbed oxygen (O_C) [25]. The Se 3d spectrum in Figure 5d shows that two characteristic peaks at about 52.6 and 53.46 eV can be assigned to Se 3d_{5/2} and Se 3d_{3/2}, respectively. The Mo 3d spectrum in Figure 5e shows that two characteristic peaks at energy band energies of 227.3 and 230.25 eV are attributed to Mo 3d_{5/2} and Mo 3d_{3/2} of the Mo⁴⁺ state in MoSe₂, respectively. Figure 5f shows the core energy level spectrum of Pd 3d. The peaks at 335.33 and 341.57 eV are assigned to Pd⁰ and Pd²⁺, respectively [23,26].

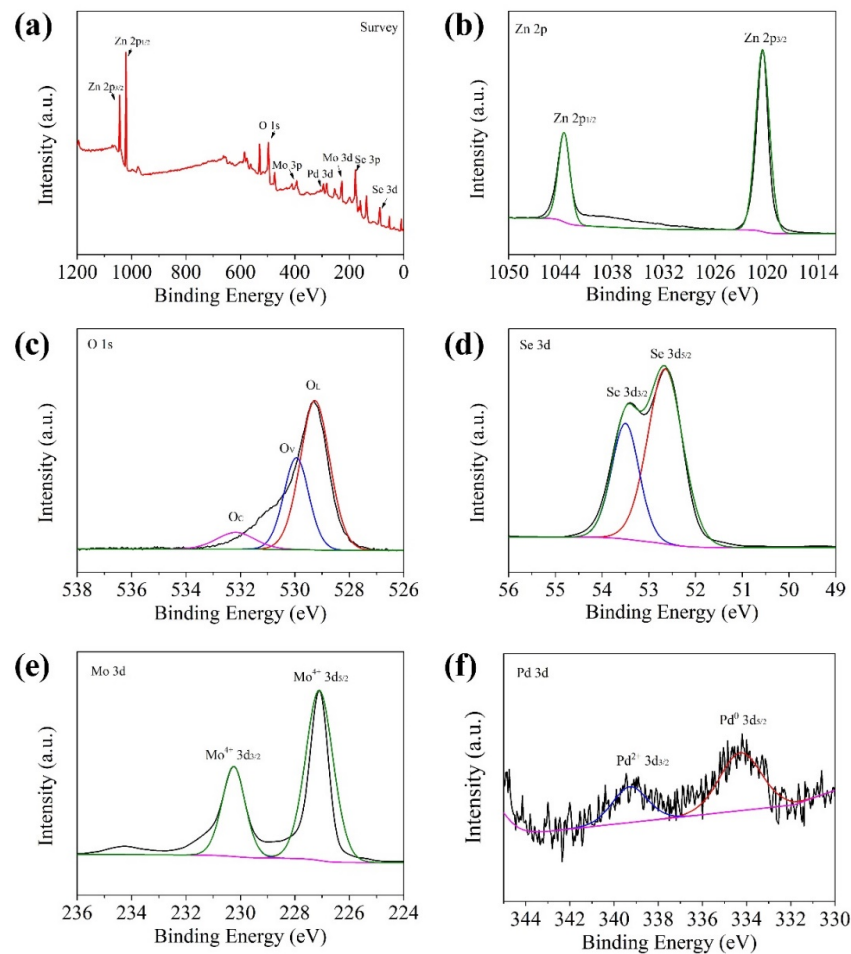


Figure 5. XPS spectra of Pd@ZnO/MoSe₂ sample: (a) full spectrum, (b) Zn 2p spectrum, (c) O 1s spectrum, (d) Se 3d spectrum, (e) Mo 3d spectrum and (f) Pd 3d spectrum.

3.3. Sensing Properties

Figure 6a illustrates the output voltage of the TENG at room temperature (RT) in air at different frequencies (2, 4, 5, 8 and 10 Hz). It can be seen from the figure that the output voltage of the TENG increases with the increase in frequency. When the frequency reaches 10 Hz, the output voltage reaches the maximum. The sum of absolute values of positive and negative voltages of TENG is about 200 V at 10 Hz. On this basis, the NO₂ sensing performances of the ZnO, Pd@ZnO and Pd@ZnO/MoSe₂ film sensors were studied by using the TENG as a power supply. Figure 6b shows the changes in output voltages of the three sensors when exposed to NO₂ gas with a concentration of 1–50 ppm at a frequency of 5 Hz. With the increase in the NO₂ concentration, the output voltage values of all the three sensors increase significantly [27,28]. When the sensors are in the air, peak-to-peak voltages of the ZnO, Pd@ZnO and Pd@ZnO/MoSe₂ sensors are 7.5 V (± 0.6 V), 2.2 V (± 0.3 V) and 2.4 V (± 0.2 V), respectively. When the sensors are in the 50 ppm NO₂, peak-to-peak voltages of the ZnO, Pd@ZnO and Pd@ZnO/MoSe₂ sensors are 33.95 V (± 2.8 V), 21.69 V (± 2.5 V) and 33.14 V (± 2.7 V), respectively. Based on the definition, the voltage responses of the three self-powered sensors at different concentrations of NO₂ gas are calculated, as shown in Figure 6c. The response of the Pd@ZnO/MoSe₂ sensor based on the TENG towards 50 ppm NO₂ gas reaches 13.8. Obviously, the response of Pd@ZnO/MoSe₂ is higher than that of ZnO and Pd@ZnO. In addition, Figure 6d shows that the response and recovery times of the Pd@ZnO/MoSe₂ sensor exposed to 1 ppm NO₂ gas are 76 and 25 s, respectively. The recovery time of the sensor is shorter than the response time, which may be because sensitive materials require less energy during desorption. At the same time, it also shows that the sensor has good recovery performance and mechanical stability. Figure 6e shows the responses of the Pd@ZnO/MoSe₂ thin-film sensor exposed to 10 ppm hydrogen sulfide, methanol, nitrogen dioxide, acetone and ammonia. The thin-film sensor has the highest response to NO₂ gas, indicating good selectivity to NO₂. In addition, Table 1 shows the comparison of the sensing performance of the NO₂ sensors prepared in this work and previously reported [29–32]. The results show that the Pd@ZnO/MoSe₂ composite film-based sensor has a high response. The sensor response in different humidity levels is shown in Figure 6f. The sensor response gradually decreases with the increase in humidity level.

Table 1. Comparison of various NO₂ sensors.

Sensor Materials	Signal Type	Concentration	Response(V_g/V_a)	Ref.
RGO/ZnO	Voltage	30 ppm	3.2	[29]
WO ₃	Voltage	30 ppm	2.5	[30]
In ₂ O ₃ /SnS ₂	Voltage	30 ppm	10.7	[31]
WO ₃ /MXene	Voltage	30 ppm	4.1	[32]
Pd@ZnO/MoSe ₂	Voltage	30 ppm	11.2	This work

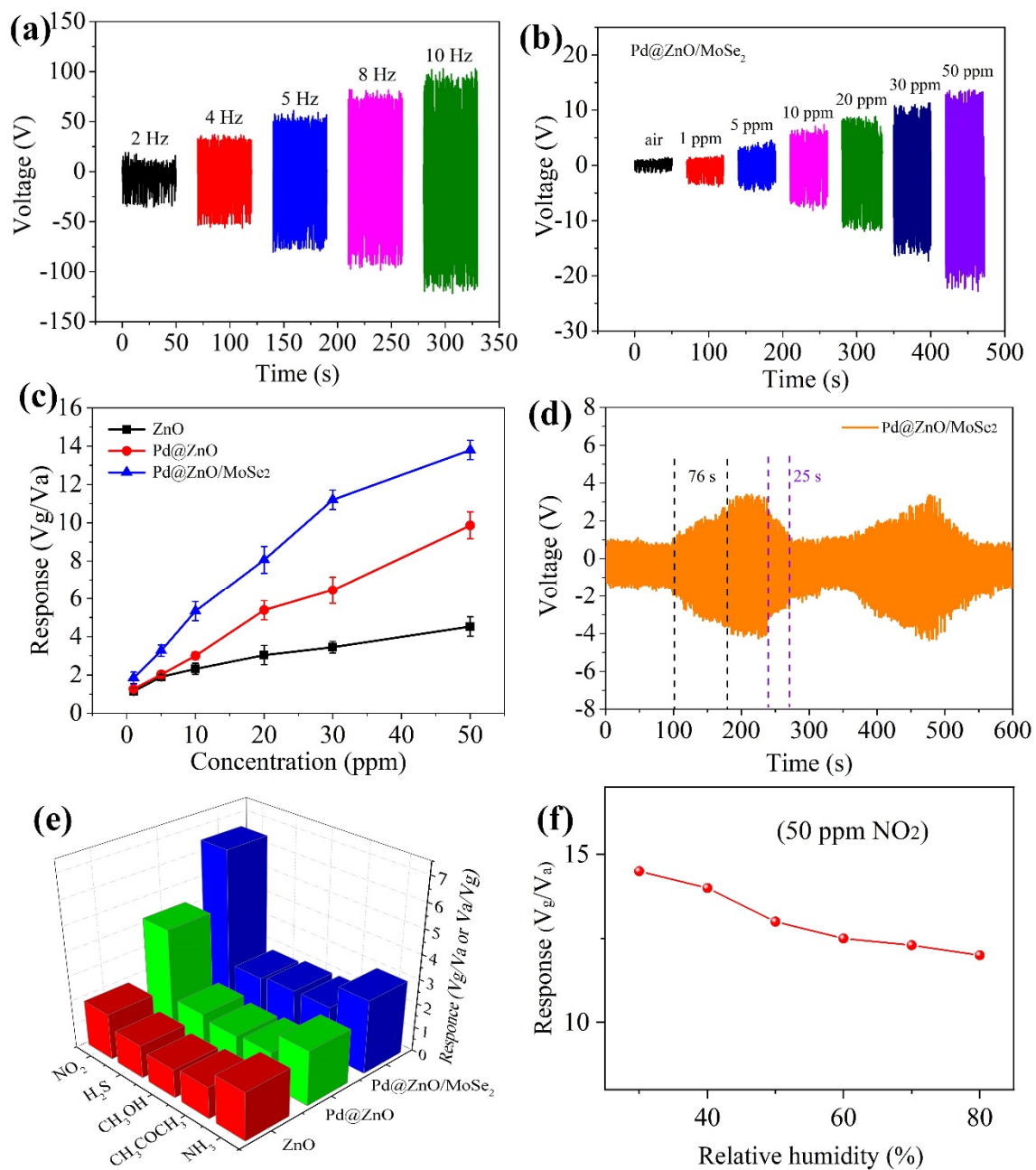


Figure 6. (a) Voltage test diagram of TENG at different frequencies at 25 °C. (b) Voltage values of Pd@ZnO/MoSe₂ exposed to different concentrations of NO₂ at 5 Hz at 25 °C. (c) Response fitting curves of ZnO, Pd@ZnO and Pd@ZnO/MoSe₂ film sensors toward different concentrations of NO₂ gas. (d) Mechanical reliability test of Pd@ZnO/MoSe₂ composite exposed to 1 ppm NO₂ at 5 Hz. (e) Response of Pd@ZnO/MoSe₂ exposed to 10 ppm nitrogen dioxide, hydrogen sulfide, methanol, acetone and ammonia. (f) The sensor response in different humidity levels.

3.4. Wearable Practical Application

It is found that the TENG can generate different energy driven by human motion. The device was placed separately on the different parts of the human body and the movement of the body part can produce a real-time voltage response. As shown in Figure 7a, the device is placed on the wrist to obtain the regular pulse signal of the human body. Figure 7b shows that the device at the joint of the index finger generates an approximate voltage signal when the finger is bent. The device was placed on the insole on the sole of the foot to observe the real-time output voltage of walking slowly (Figure 7c) and running (Figure 7d).

Running can generate about 7 V voltage signal, which provides a new idea for the research of self-powered wearable devices.

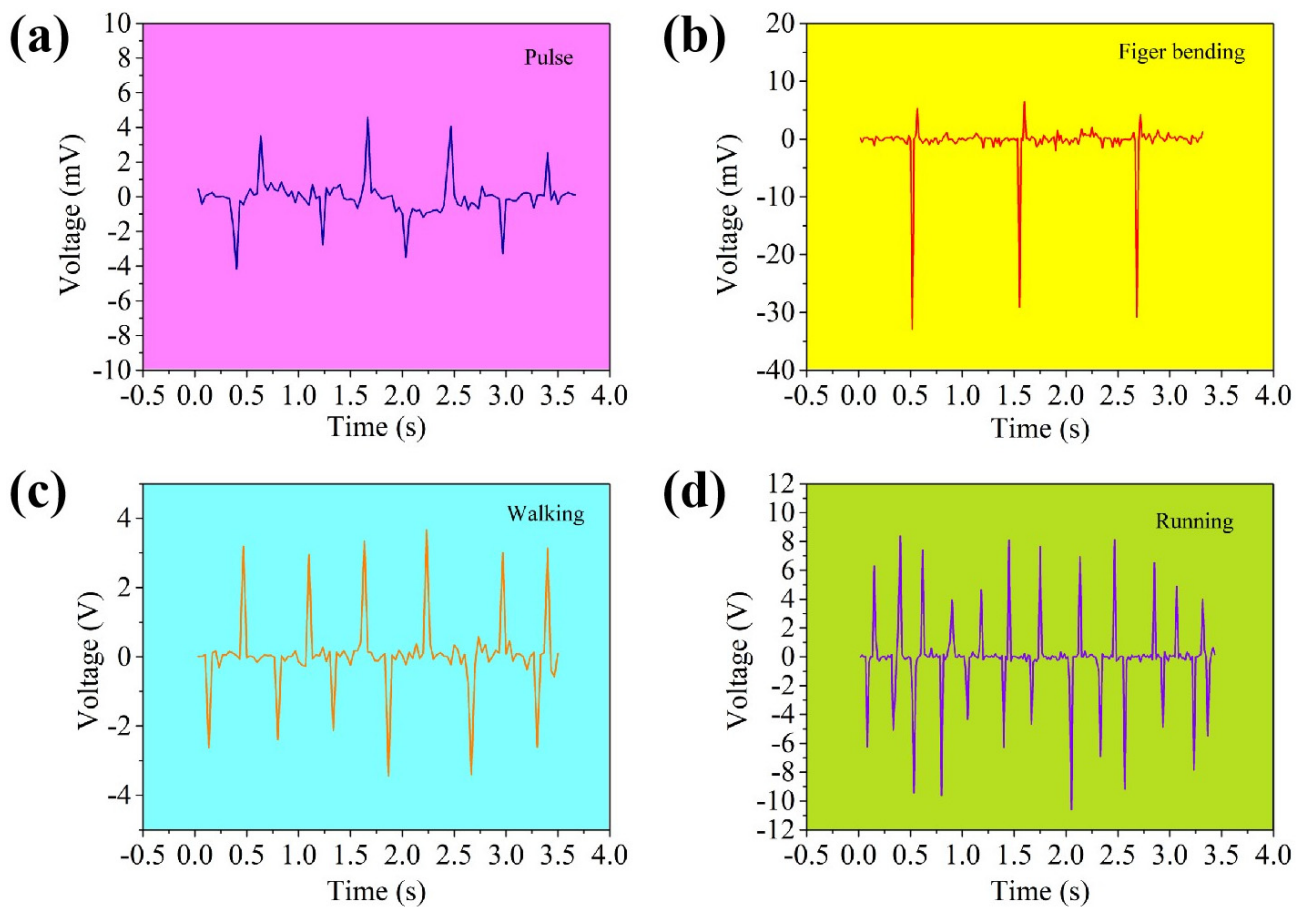


Figure 7. Wearable nanogenerator based on TENG at 25 °C: (a) placed on the wrist for weak pulse signals, (b) placed on the index knuckle to bend and clench and (c,d) placed on the sole of the foot to walk and run to generate energy.

4. NO₂ Sensing Mechanism

Figure 8a shows the I–V curves of ZnO, MoSe₂, Pd@ZnO and ZnO/MoSe₂ thin films. The I–V characteristic curve of the Pd@ZnO sensor shows obvious nonlinearity between –4 and 4 V, which reveals the good Schottky contact between ZnO nanoparticles and Pd. The slope of the I–V curve also shows that the conductivity of the Pd@ZnO sensing film is much higher than that of ZnO [33]. Pd nanoparticles dispersed on the surfaces of nanocomposites can enhance the availability of active sites for gas adsorption, which is conducive to gas adsorption. At the same time, ZnO/MoSe₂ thin films have better nonlinearity than single ZnO and MoSe₂, which indicates that the heterojunction has better rectification performance [34].

From the experimental results, we can find that the response of the Pd@ZnO/MoSe₂ composite thin-film-based sensor to NO₂ gas is obviously improved at room temperature. The gas-sensing mechanism of semiconductors can be explained by the chemical adsorption of gas molecules and the electron exchange caused by oxygen adsorption [35]. Figure 8b,c show the Pd@ZnO/MoSe₂ sensing mechanism in air and NO₂ gas at room temperature. When the sensor is exposed to the air, oxygen molecules in the air will be adsorbed on the surface of the sensing material [36]. The oxygen molecules capture electrons and produce chemically adsorbed oxygen anions (O₂[–]).

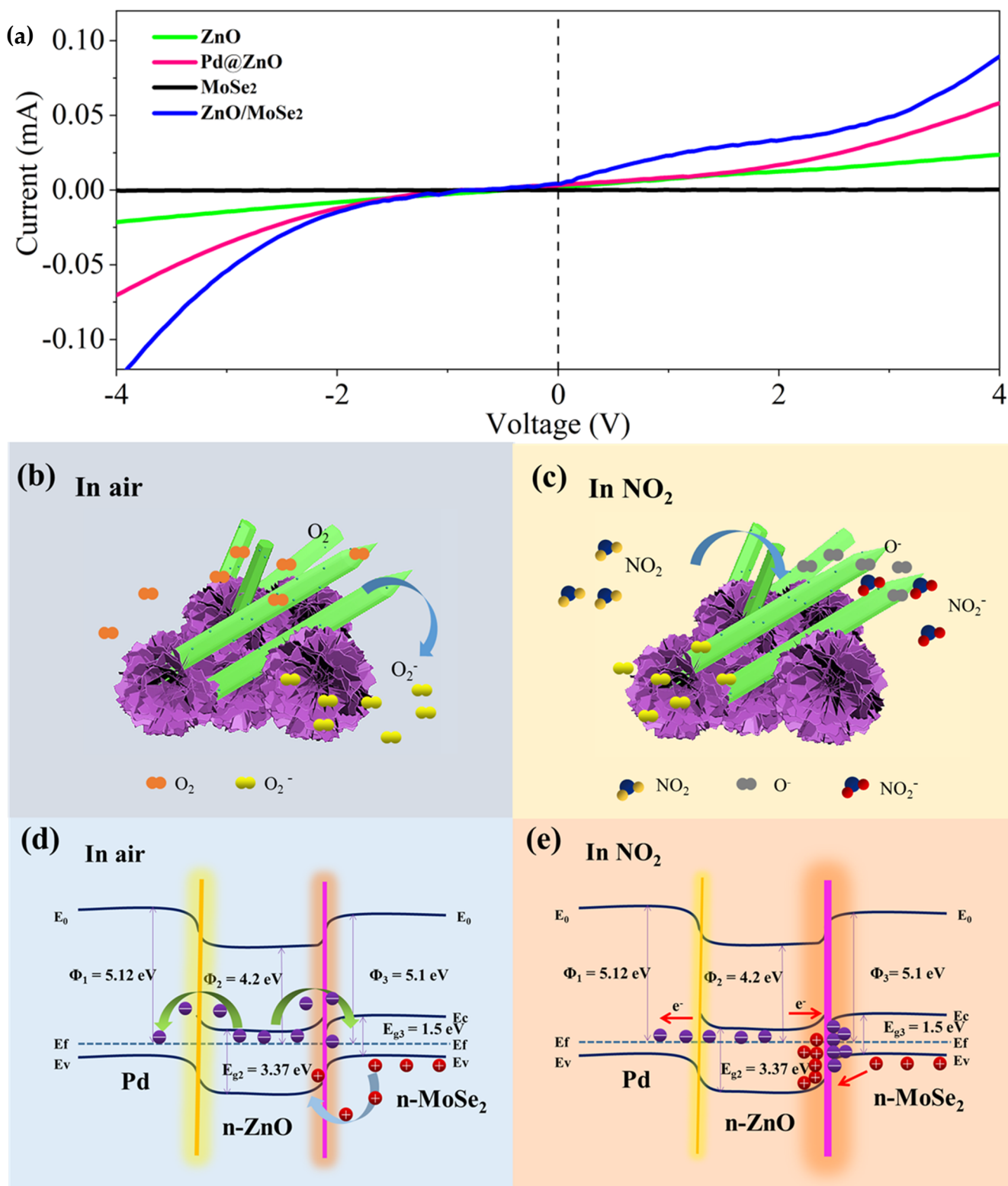
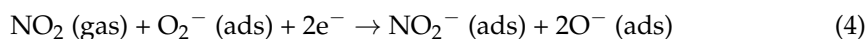
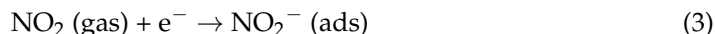


Figure 8. (a) I–V curve of ZnO, MoSe₂, Pd@ZnO and ZnO/MoSe₂ at 25 °C. (b,c) Gas-sensing mechanism of Pd@ZnO/MoSe₂ composites in air and NO₂. (d,e) Energy band structure of Pd@ZnO/MoSe₂ composites in air and NO₂ (E_f, Fermi-energy level; E_C, conduction band; E_V, valence band; φ, work function).

When the sensor is exposed to NO₂ gas, the highly electrophilic NO₂ molecules extract electrons directly from the sensing layer and react with O₂⁻, resulting in an increase in

sensor resistance. When the sensor is switched to the air, the electrons trapped by NO₂ molecules are released back to the conductive band of the material, causing the resistance to return to its initial state. The process is as follows [32]:



ZnO and MoSe₂ are n-type semiconductor materials, which are characterized by electronic conductivity, and the work functions are 4.2 and 5.1 eV, respectively [23,37]. Pd is a metal material with a work function dimension of 5.12 eV [19]. Therefore, the sensing mechanism shown in Figure 8d,e can be attributed to the Pd@ZnO/MoSe₂ Schottky barrier and n–n heterostructure interaction. The work function of Pd NPs is larger than that of ZnO and electrons will transfer from ZnO to Pd until their Fermi level is balanced. In air, electrons gather around palladium nanoparticles. When exposed to NO₂ gas, the electrons are released, resulting in electron depletion layer thinning and sensor resistance reduction. Due to the existence of palladium nanoparticles, electron transfer is easier to achieve and improves the sensor response. This will greatly improve the sensing performance of the Pd@ZnO/MoSe₂ nanocomposite sensor. The n–n heterojunction formed at the interface between ZnO and MoSe₂ may be another key factor in improving the sensing performance of NO₂ [38]. When ZnO and MoSe₂ contact, a heterojunction is formed at their contact interfaces. Because the work function of MoSe₂ is larger than that of ZnO, electrons will be transferred from ZnO to MoSe₂ until the Fermi level is balanced. The electron depletion layer and the electron accumulation layer are formed at the interfaces of ZnO and MoSe₂, respectively. When exposed to NO₂ gas, the carrier concentration in the heterojunction further decreases, which leads to a broadening of the depletion layer at the ZnO/MoSe₂ interface, which is beneficial to the improvement in the sensing performance of the Pd@ZnO/MoSe₂ nanocomposite sensor.

5. Conclusions

The TENG was prepared by using Al-PVA and PI, and a self-powered room temperature NO₂ sensor was developed. By converting mechanical motion into electrical energy, the TENG could be used as a power source for driving sensors. The output voltage signals of sensors exposed to NO₂ gas were tested under 5 Hz. Experimental results showed that, compared with single ZnO and Pd@ZnO, the TENG-driven Pd@ZnO/MoSe₂ sensor had high sensitivity and good selectivity. The enhanced sensing properties may be due to the formations of a Schottky junction and n–n heterojunction on the contact interfaces of Pd, ZnO and MoSe₂. This work promotes the research of a self-powered gas sensor and has important significance for environmental monitoring.

Author Contributions: Conceptualization, W.W. and D.Z.; methodology, D.Z.; validation, X.Z., D.W. and C.Y.; formal analysis, X.Z.; investigation, W.W.; data curation, D.W.; writing—original draft preparation, C.Y.; writing—review and editing, D.Z. and D.W. All authors have read and agreed to the published version of the manuscript.

Funding: This work was supported by the National Natural Science Foundation of China (51777215, 42176083).

Data Availability Statement: Not applicable.

Conflicts of Interest: The authors declare no conflict of interest.

References

1. Liu, H.; Xu, Y.; Zhang, X.; Zhao, W.; Ming, A.; Wei, F. Enhanced NO₂ sensing properties of Pt/WO₃ films grown by glancing angle deposition. *Ceram. Int.* **2020**, *46*, 21388–21394. [[CrossRef](#)]
2. Zhang, C.; Huan, Y.; Sun, D.; Lu, Y. Synthesis and NO₂ sensing performances of CuO nanoparticles loaded In₂O₃ hollow spheres. *J. Alloys Compd.* **2020**, *842*, 155857. [[CrossRef](#)]
3. Zhang, J.; Wu, J.; Wang, X.; Zeng, D.; Xie, C. Enhancing room-temperature NO₂ sensing properties via forming heterojunction for NiO-rGO composited with SnO₂ nanoplates. *Sens. Actuators B* **2017**, *243*, 1010–1019. [[CrossRef](#)]
4. Khojier, K.; Savaloni, H.; Habashi, N.; Sadi, M.H. On the influence of temperature gradient of annealing process on the nanostructure and sensing properties of WO₃ thin films to NO₂ gas and relative humidity. *Mater. Sci. Semicond. Process.* **2016**, *41*, 177–183. [[CrossRef](#)]
5. Wang, D.; Zhang, D.; Yang, Y.; Mi, Q.; Zhang, J.; Yu, L. Multifunctional latex/polytetrafluoroethylene-based triboelectric nanogenerator for self-powered organ-like MXene/metal–organic framework-derived CuO nanohybrid ammonia sensor. *ACS Nano* **2021**, *15*, 2911–2919. [[CrossRef](#)]
6. Cheng, Z.; Song, L.; Ren, X.; Zheng, Q.; Xu, J. Novel lotus root slice-like self-assembled In₂O₃ microspheres: Synthesis and NO₂-sensing properties. *Sens. Actuators B* **2015**, *176*, 258–263. [[CrossRef](#)]
7. Hermawan, A.; Septiani, N.; Taufik, A.; Yuliarto, B.; Suyatman; Yin, S. Advanced strategies to improve performances of molybdenum-based gas sensors. *Nano-Micro Lett.* **2021**, *13*, 207. [[CrossRef](#)]
8. Fan, X.; He, J.; Mu, J.; Qian, J.; Zhang, N.; Yang, C.; Hou, X.; Geng, W.; Wang, X.; Chou, X. Triboelectric-electromagnetic hybrid nanogenerator driven by wind for self-powered wireless transmission in Internet of Things and self-powered wind speed sensor. *Nano Energy* **2020**, *68*, 104319. [[CrossRef](#)]
9. Fan, F.; Tian, Z.; Wang, Z. Flexible triboelectric generator. *Nano Energy* **2012**, *1*, 328–334. [[CrossRef](#)]
10. Wang, S.; Xie, G.; Tai, H.; Su, Y.; Yang, B.; Zhang, Q.; Du, X.; Jiang, Y. Ultrasensitive flexible self-powered ammonia sensor based on triboelectric nanogenerator at room temperature. *Nano Energy* **2018**, *51*, 231–240. [[CrossRef](#)]
11. Han, W.; He, H.; Zhang, L.; Dong, C.; Zeng, H.; Dai, Y.; Xing, L.; Zhang, Y. A self-powered wearable noninvasive electronic-skin for perspiration analysis based on piezo-biosensing unit matrix of enzyme/ZnO nanoarrays. *ACS Appl. Mater. Interfaces* **2017**, *9*, 29526–29537. [[CrossRef](#)] [[PubMed](#)]
12. Liu, D.; Zhou, L.; Cui, S.; Gao, Y.; Li, S.; Zhao, Z.; Yi, Z.; Zou, H.; Fan, Y.; Wang, J.; et al. Standardized measurement of dielectric materials intrinsic triboelectric charge density through the suppression of air breakdown. *Nat. Commun.* **2022**, *13*, 6019. [[CrossRef](#)] [[PubMed](#)]
13. Seung, W.; Yoon, H.J.; Kim, T.Y.; Ryu, H.; Kim, J.; Lee, J.H.; Lee, J.H.; Kim, S.; Park, Y.K.; Park, Y.J.; et al. Boosting power-generating performance of triboelectric nanogenerators via artificial control of ferroelectric polarization and dielectric properties. *Adv. Energy Mater.* **2017**, *7*, 1600988. [[CrossRef](#)]
14. Zhang, H.; Zhang, D.; Zhang, B.; Wang, D.; Tang, M. Wearable pressure sensor array with layer-by-layer assembled MXene nanosheets/Ag nanoflowers for motion monitoring and human–machine Interfaces. *ACS Appl. Mater. Interfaces* **2022**, *14*, 48907–48916. [[CrossRef](#)] [[PubMed](#)]
15. Wang, D.; Zhang, D.; Chen, X.; Zhang, H.; Tang, M.; Wang, J. Multifunctional respiration-driven triboelectric nanogenerator for self-powered detection of formaldehyde in exhaled gas and respiratory behavior. *Nano Energy* **2022**, *102*, 107711. [[CrossRef](#)]
16. Jiang, C.; Wu, C.; Li, X.; Yao, Y.; Lan, L.; Zhao, F.; Ye, Z.; Ying, Y.; Ping, J. All-electrospun flexible triboelectric nanogenerator based on metallic MXene nanosheets. *Nano Energy* **2019**, *59*, 268–276. [[CrossRef](#)]
17. Wang, D.; Zhang, D.; Tang, M.; Zhang, H.; Sun, T.; Yang, C.; Mao, R.; Li, K.; Wang, J. Ethylene chlorotrifluoroethylene/hydrogel-based liquid-solid triboelectric nanogenerator driven self-powered MXene-based sensor system for marine environmental monitoring. *Nano Energy* **2022**, *100*, 107509. [[CrossRef](#)]
18. Heckova, M.; Streckova, M.; Orinakova, R.; Hovancova, J.; Gubova, A.; Sopcak, T.; Kovalcikova, A.; Plesingerova, B.; Medved, D.; Szabo, J.; et al. Porous carbon fibers for effective hydrogen evolution. *Appl. Surf. Sci.* **2020**, *506*, 144955. [[CrossRef](#)]
19. Diouri, N.; Baitoul, M. Effect of carbon nanotubes dispersion on morphology, internal structure and thermal stability of electrospun poly(vinyl alcohol)/carbon nanotubes nanofibers. *Opt. Quantum Electron.* **2014**, *46*, 259–269. [[CrossRef](#)]
20. Wang, D.; Zhang, D.; Li, P.; Yang, Z.; Mi, Q.; Yu, L. Electrospinning of flexible poly(vinyl alcohol)/MXene nanofiber-based humidity sensor self-powered by monolayer molybdenum diselenide piezoelectric nanogenerator. *Nano-Micro Lett.* **2021**, *13*, 57. [[CrossRef](#)]
21. Wang, D.; Zhang, D.; Mi, Q. A high-performance room temperature benzene gas sensor based on CoTiO₃ covered TiO₂ nanospheres decorated with Pd nanoparticles. *Sens. Actuators B* **2022**, *350*, 130830. [[CrossRef](#)]
22. Li, W.; Li, X.; Chen, Y.; Li, X.; Deng, H.; Wang, T.; Huang, R.; Fan, G. Poly(vinyl alcohol)/sodium alginate/layered silicate based nanofibrous mats for bacterial inhibition. *Carbohydr. Polym.* **2013**, *92*, 2232–2238. [[CrossRef](#)] [[PubMed](#)]
23. Gu, F.; Chen, H.; Han, D.; Wang, Z. Metal-organic framework derived Au@ZnO yolk-shell nanostructures and their highly sensitive detection of acetone. *RSC Adv.* **2016**, *6*, 29727–29733. [[CrossRef](#)]
24. Hassan, K.; Chung, G. Catalytically activated quantum-size Pt/Pd bimetallic core–shell nanoparticles decorated on ZnO nanorod clusters for accelerated hydrogen gas detection. *Sens. Actuators B* **2017**, *239*, 824–833. [[CrossRef](#)]
25. Xu, M.; Yu, R.; Guo, Y.; Chen, C.; Han, Q.; Di, J.; Song, P.; Zheng, L.; Zhang, Z.; Yan, J.; et al. New strategy towards the assembly of hierarchical heterostructures of SnO₂/ZnO for NO₂ detection at a ppb level. *Inorg. Chem. Front.* **2019**, *6*, 2801–2809. [[CrossRef](#)]

26. Liu, H.; Guo, H.; Liu, B.H.; Liang, M.F.; Lv, Z.L.; Adair, K.R.; Sun, X.L. Few-layer MoSe₂ nanosheets with expanded (002) planes confined in hollow carbon nanospheres for ultrahigh-performance Na-ion batteries. *Adv. Funct. Mater.* **2018**, *28*, 1707480. [[CrossRef](#)]
27. Zhang, C.; Luo, Y.; Xu, J.; Debliquy, M. Room temperature conductive type metal oxide semiconductor gas sensors for NO₂ detection. *Sens. Actuators A* **2019**, *289*, 118–133. [[CrossRef](#)]
28. Fu, Y.; He, H.; Zhao, T.; Dai, Y.; Han, W.; Ma, J.; Xing, L.; Zhang, Y.; Xue, X. A self-powered breath analyzer based on PANI/PVDF piezo-gas-sensing arrays for potential diagnostics application. *Nano-Micro Lett.* **2018**, *10*, 76. [[CrossRef](#)]
29. Su, Y.; Xie, G.; Tai, H.; Li, S.; Yang, B.; Wang, S.; Zhang, Q.; Du, H.; Zhang, H.; Du, X.; et al. Self-powered room temperature NO₂ detection driven by triboelectric nanogenerator under UV illumination. *Nano Energy* **2018**, *47*, 316–324. [[CrossRef](#)]
30. Su, Y.; Wang, J.; Wang, B.; Yang, T.; Yang, B.; Xie, G.; Zhou, Y.; Zhang, S.; Tai, H.; Cai, Z.; et al. Alveolus-inspired active membrane sensors for self-powered wearable chemical sensing and breath analysis. *ACS Nano* **2020**, *14*, 6067–6075. [[CrossRef](#)]
31. Yang, Y.; Zhang, D.; Wang, D.; Xu, Z.; Zhang, J. A high-stability weighing paper/polytetrafluoroethylene-based triboelectric nanogenerator for self-powered In₂O₃ nanocubes/SnS₂ nanoflower NO₂ gas sensors. *J. Mater. Chem. A* **2021**, *9*, 14495. [[CrossRef](#)]
32. Wang, D.; Zhang, D.; Guo, J.; Hu, Y.; Yang, Y.; Sun, T.; Zhang, H.; Liu, X. Multifunctional poly(vinyl alcohol)/Ag nanofibers-based triboelectric nanogenerator for self-powered MXene/tungsten oxide nanohybrid NO₂ gas sensor. *Nano Energy* **2021**, *89*, 106410. [[CrossRef](#)]
33. Kaufmanna, B.; Raidl, N.; Supancic, P. Investigation of schottky barriers at Pd-ZnO junctions in varistors. *J. Eur. Ceram. Soc.* **2020**, *40*, 3771–3775. [[CrossRef](#)]
34. Chang, X.; Qiao, X.; Li, K.; Wang, P.; Xiong, Y.; Li, X.; Xia, F.; Xue, Q. UV assisted ppb-level acetone detection based on hollow ZnO/MoS₂ nanosheets core/shell heterostructures at low temperature, *Electron. Sens. Actuators B* **2020**, *317*, 128208. [[CrossRef](#)]
35. Sun, C.; Dutta, P.K. Selective detection of part per billion concentrations of ammonia using a pen semiconducting oxide heterostructure. *Sens. Actuators B* **2016**, *226*, 156–169. [[CrossRef](#)]
36. Zhao, S.; Shen, Y.; Yan, X.; Zhou, P.; Yin, Y.; Lu, R.; Han, C.; Cui, B.; Wei, W. Complex-surfactant-assisted hydrothermal synthesis of one-dimensional ZnO nanorods for high-performance ethanol gas sensor. *Sens. Actuators B* **2019**, *286*, 501–511. [[CrossRef](#)]
37. Kim, J.H.; Mirzaei, A.; Kim, H.W.; Kim, S.S. Low power-consumption CO gas sensors based on Au-functionalized SnO₂-ZnO core-shell nanowires. *Sens. Actuators B* **2018**, *267*, 597–607. [[CrossRef](#)]
38. Wang, Z.; Gao, S.; Fei, T.; Liu, S.; Zhang, T. Construction of ZnO/SnO₂ heterostructure on reduced graphene oxide for enhanced nitrogen dioxide sensitive performances at room temperature. *ACS Sens.* **2019**, *4*, 2048–2057. [[CrossRef](#)]